CiGNN: A Causality-Informed and Graph Neural Network Based Framework for Cuffless Continuous Blood Pressure Estimation

Lei Liu, *Student Member, IEEE*, Huiqi Lu, *Member, IEEE*, Maxine Whelan, Yifan Chen, *Senior Member, IEEE*, and Xiaorong Ding, *Member, IEEE*

***Abstract*—Causalityholds profound potentials to dissipate confusion and improve accuracy in cuffless continuous blood pressure (BP) estimation, an area often neglected in current research. In this study, we propose a two-stage framework, CiGNN, that seamlessly integrates causality and graph neural network (GNN) for cuffless continuous BP estimation. The first stage concentrates on the generation of a causal graph between BP and wearable features from the the perspective of causal inference, so as to identify features that are causally related to BP variations. This stage is pivotal for the identification of novel causal features from the causal graph beyond pulse transit time (PTT). We found these causal features empower better tracking in BP changes compared to PTT. For the second stage, a spatio-temporal GNN (STGNN) is utilized to learn from the causal graph obtained from the first stage. The STGNN can exploit both the spatial information within the causal graph and temporal information from beat-by-beat cardiac signals for refined cuffless continuous BP estimation. We evaluated the proposed method with three datasets that include 305 subjects (102 hypertensive patients) with age ranging from 20–90 and BP at different levels, with the continuous Finapres BP as references. The mean absolute difference (MAD) for estimated systolic blood pressure (SBP) and diastolic blood pressure (DBP) were 3.77 mmHg and 2.52 mmHg, respectively, which outperformed comparison methods. In all cases including subjects with different age groups, while doing various maneuvers that induces BP changes at different levels and with or without hypertension, the proposed CiGNN method demonstrates superior performance for cuffless continuous BP estimation. These findings suggest that the proposed CiGNN is a promising approach in elucidating the causal mechanisms of cuffless BP estimation and can substantially enhance the precision of BP measurement.**

***Index Terms*—Amplitude alteration, Causality, cuffless continuous blood pressure, pulse transit time, spatio-temporal graph neural network.**

I. Introduction

ACCORDING to the World Health Organization (WHO), approximately 1.13 billion individuals worldwide suffer from hypertension, with this an expected increase to 1.5 billion by 2025 [1]. Hypertension, or high blood pressure, is a prominent risk factor for cardiovascular diseases, including heart disease and stroke, which are leading causes of death globally [2]. The prevalence of hypertension would further increase the existing burdens of dementia and disability worldwide [3]. Therefore, effective prevention and management of hypertension are crucial for improving global health outcomes.

Continuous BP measurement has the potential to provide rich information for the diagnosis and prevention of hypertension [4]. By monitoring BP continuously, we can obtain a more comprehensive understanding of a patient's BP over time, as the patterns and trends in BP can indicate the need for treatment or adjustments in current treatment plans. In addition, continuous BP monitoring has an advantage over conventional intermittent BP measurement, because BP may be influenced by factors such as stress, physical activity, and medication adherence. For example, continuous BP measurement can overcome the clinical "white coat effect" - the phenomenon of elevated BP readings in a clinical setting - and provides more accurate and reliable readings [5].

Cuffless continuous BP measurement enabled by wearable physiological sensing has emerged as a promising approach for its advantage of being noninvasive, its ease of use, and continuous nature [6]. With BP changes-related features extracted from wearable cardiac signals, such as electrocardiogram (ECG) and photoplethysmogram (PPG), models can be developed to map the features to BP so as to achieve an indirect estimation. Cuffless BP estimation models can be broadly classified into two categories: knowledge-driven model and data-driven model.

The knowledge-driven models rely on expert knowledge of the cardiovascular system. For instance, Chen et al. developed a

Manuscript received 30 October 2023; revised 27 January 2024; accepted 4 March 2024. Date of publication 13 March 2024; date of current version 7 May 2024. This work was supported in part by the Sichuan Science and Technology Program under Grant 2021YFH0179, and in part by the National Natural Science Foundation of China under Grant 82102178. The work of Huiqi Lu was supported in part by the Royal Academy of Engineering Daphne Jackson Trust Fellowship grant, an EPSRC Healthcare Technologies Challenge Award under Grant EP/N020774/1 and in parrt by Wellcome Trust under Grant 217650/Z/19/Z. *(Corresponding author: Xiaorong Ding.)*

Lei Liu, Yifan Chen, and Xiaorong Ding are with the School of Life Science and Technology, University of Electronic Science and Technology of China, Chengdu 611731, China (e-mail: xiaorong.ding@uestc.edu.cn).

Huiqi Lu is with the Institute of Biomedical Engineering, University of Oxford, OX1 2JD Oxford, U.K.

Maxine Whelan is with the Centre for Healthcare and Communities, Coventry University, CV1 5FB Coventry, U.K.

This article has supplementary downloadable material available at https://doi.org/10.1109/JBHI.2024.3377128, provided by the authors.

Digital Object Identifier 10.1109/JBHI.2024.3377128

physiological model for cuffless BP estimation based on pulse transit time (PTT) and the Moens-Korteweg (M-K) equation [7]. Ding et al. built a more comprehensive physiological model that considers M-K equation and Windkess model with the combination of PTT and PPG Intensity Ratio (PIR) [8]. However, these mechanism models usually work with underlying assumptions that may not be true. Taking the M-K equation for example, it assumes that the artery wall is isotropic and experiences isovolumetric change with pulse pressure, which is not the case in human beings. These impractical assumptions can lead to inaccuracies in BP estimation [9].

Data-driven models, on the other hand, involve learning the mapping function from BP-related information to BP from data [10]. For example, Miao et al. [11] employed deep learning module, such as ResNet and long short-term memory (LSTM) models, to estimate cuffless BP from PPG signal. Tanveer et al. proposed an artificial neural network integrated with the LSTM model to estimate cuffless BP from both ECG and PPG signals [12]. Though advances in machine learning (ML) techniques provide new inspirations for cuffless BP estimation, the limitations of ML, such as the generalization issue, also hinder the development of data-driven methods for further clinical implementation. Data-driven methods depend on large amounts of high-quality data, which could be difficult and costly to acquire. Their performance can also be affected by confounding factors such as motion artifacts and environmental noise. Moreover, the black-box nature of ML can make it challenging to interpret the underlying physiological mechanisms and identify potential sources of inaccuracy [13].

The key to accurate continuous cuffless BP estimation includes the wearable features/information that have causal association with BP changes and the model that can relate the appropriate features/information with BP. However, most of the current studies that focus on either knowledge-driven or data-driven methods overlook the causal relationships between wearable features and BP changes, and the underlying causes or effects of BP changes have rarely been identified. Causality has the potential to improve the interpretability, robustness, and generalizability of cuffless BP estimation methods [14]. Further, it can help identify the underlying mechanisms for cuffless BP measurement, allowing for more accurate predictions [15].

Pearl has put forward the theory of Bayesian networks and causal inference using causal graphs to describe the causal relationships between multi-variables [16]. Intuitively in the causal graph, each node represents a random variable and the directed edges between nodes reveal the data generation process or the relationship of cause and effect between nodes. The problem of inferring causal relationships from purely observed data has drawn significant attention in recent years [17]. Common methods developed for causal inference includes constraint-based algorithms, score-based algorithms and Functional Causal Models (FCM) based algorithms [18].

Constraint-based algorithm infers the causal graph by imposing conditional independence constraints among the variables, and the algorithm is computationally efficient and able to handle large datasets [19]. However, it supposes that the data satisfy the faithfulness assumption, which may not always be true in practice. Score-based algorithm searches for the causal graph that maximizes a score based on the likelihood of the observed data. It does not rely on the faithfulness assumption but can be computationally expensive [20]. FCM-based algorithm, assuming independent non-Gaussian noise across nodes in the causal graph, utilizes independent components analysis (ICA) to recover the causal relation [21].

In our previous work, we identified the causal graph between wearable physiological features and BP with constraint-based algorithm [14]. However, due to the inherent limitations of the algorithm, the direction of some edges in the identified graph could not explicitly be oriented, which results in the only inference of a Markov equivalence class. In addition, the study employed the knowledge of causal graphs to build a cuffless BP estimation model based on time-lagged causal links [22]. Nevertheless, the time-lagged causal links only represent guiding information about the topological structure of the causal graph.

Graph neural network (GNN) is promising to address tasks on graph-structured data, such as protein interaction prediction and traffic flow forecasting [23]. GNN consists of a series of neural network layers that are applied to the nodes and edges of a graph, allowing for capturing the topological structure of the graph and incorporating it into the learning process. GNNs can learn how to propagate information across the graph, allowing each node to take into account the features and connections of its neighbouring nodes. As a result, it enables the prediction of labels or values for the entire graph. We propose a new framework for cuffless continuous BP estimation based on GNN with the identified causal graph as prior knowledge. With the topology of the causal graph indicating the causal association between wearable features and BP, we expect the GNN can derive a causal representation for BP estimation.

This proposed causality-informed and graph neural network based (CiGNN) framework for cuffless continuous BP estimation consists of two stages. In stage I, we infer the causal graph between extracted wearable features and BP with an improved causal inference algorithm to address the issue of Markov equivalence class. In stage II, a spatio-temporal graph neural network (STGNN) model is developed to learn representations from the causal graph. The STGNN model can capture both the spatial and temporal information for cuffless continuous BP estimation. The main contributions of this paper include:

- Development of an FCM-based algorithm that enables the orientation and modification of the initial causal graph, which can achieve better causal inference performance than the constraint-based algorithm.
- A STGNN model is introduced to extract the spatial information within the causal graph and temporal information from the proceeding cardiac beats for cuffless continuous BP estimation.
- The proposed two-stage CiGNN framework successfully draws novel causal insights from wearable features that can estimate cuffless continuous BP with satisfactory performance.

II. Methods

As illustrated in Fig. 1, CiGNN composes two main modules: causal inference module and a BP estimation module. The

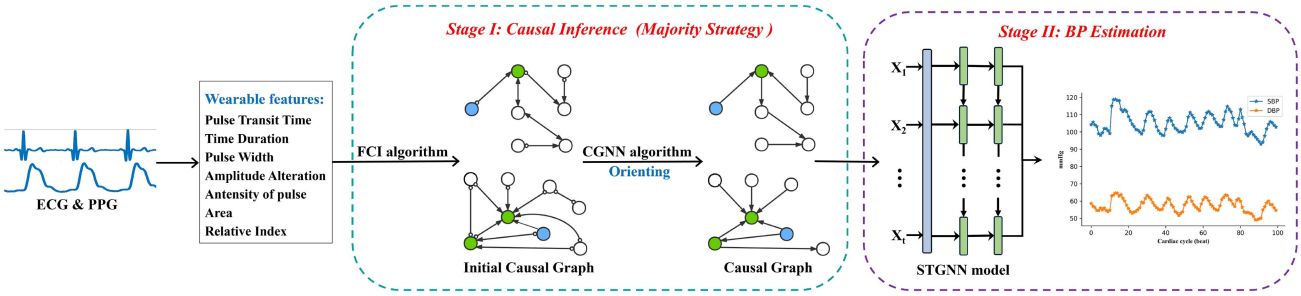

Fig. 1. Overview of the proposed causality-informed and graph neural network based (CiGNN) framework for cuffless continuous BP estimation. The wearable features are extracted initially from electrocardiogram (ECG) and photoplethysmogram (PPG). Subsequently, within the first stage, the causality between BP and wearable features is inferred by fast causal inference (FCI) and causal generative network (CGNN) algorithms. Finally, the second stage proposes the spatio-temporal graph neural network (STGNN) model, taking the causal graph sequence as its input for cuffless continuous BP estimation.

function of the first module is to infer the causal graph that relates BP with features extracted from wearable ECG and PPG signals, following the majority strategy of causal inference. An initial causal graph is identified with the fast causal inference (FCI) algorithm [24], where the direction of some edges is not oriented. Subsequently, the causal generative neural networks (CGNN) algorithm is utilized to orient and modify the direction for the initial causal graph [25]. In stage II, the directed causal graph serves as prior knowledge. An STGNN model, taking the causal graph sequence as its input, is proposed to capture both the spatial and temporal information for cuffless continuous BP estimation.

A. Datasets and Wearable Features Extraction

1) Datasets: In this study, we used **one internal dataset** for the causal inference and **two extra datasets** to evaluate the performance of the proposed CiGNN framework for BP estimation. The internal dataset utilized in this study originates from our preceding study [26], which involves 62 participants (36 males). In the dataset, the average age is 26.7 $\pm$ 4.5 years (ranging from 21 to 42 years). We collected wearable ECG and PPG signals via the Biopac system in the experiment, and the continuous BP measurement was synchronously recorded as a reference using the Finpres device. All tests were conducted with participants maintaining a seating position, where signals were acquired for 10 minutes at a sampling rate of 1000 Hz. The collective mean SBP is 114.0 $\pm$ 13.4 mmHg, accompanied with the corresponding mean DBP of 67.0 $\pm$ 10.6 mmHg. We used dataset collected from previous study [26], which has been approved by relevant Institutional Ethics Committee.

In order to validate the robustness of our proposed method, we evaluate its performance on two extra datasets: **i)** VitalDB dataset [27] has been used as the first extra dataset to collect PPG, ECG and the simultaneous invasive arterial BP (ABP). Data of 205 patients belonging to different age and BP groups have been collected and preprocessed. Tables VI and VII present brief statistical information of the selected patients. **ii)** And for validating the CiGNN's ability of tracking BP changes due to external interventions, we employed the second extra dataset [28] with a total of 38 subjects. This dataset consists of the ECG, PPG and continuous BP with subjects under four various maneuvers that can induce BP changes at different levels. The maneuvers include sit (SIT), deep breathing (DB), supine (SUP) and active standing (AS).

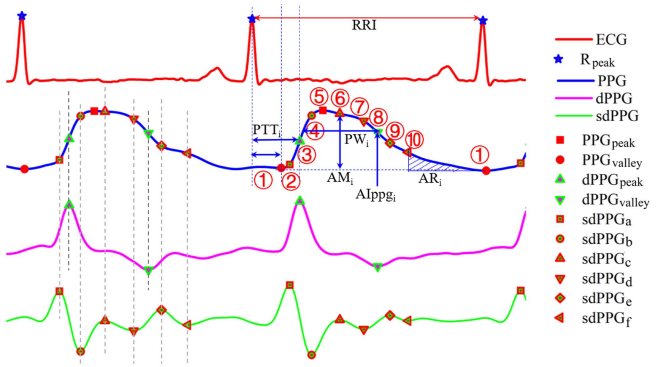

Fig. 2. Fiducial points of ECG, PPG, the first derivative of PPG (dPPG) and the second derivative of PPG (sdPPG) for feature extraction, along with the indication of several major features [7].

2) Wearable Features Extraction: To unravel the causal relationship between wearable features and BP variations within the cardiovascular system, we extract a comprehensive set of features from ECG and PPG signals, building upon our previous endeavors [29]. In total of two hundred and twenty-two wearable features across 7 categories are extracted to facilitate the subsequent causal inference. The detailed elucidation of the 222 wearable features' definitions and categorization are presented in Table I.

Fig. 2 illustrates the identified reference points on ECG, PPG, the first derivative of PPG (dPPG), and the second derivative of PPG (sdPPG) signals. The corresponding wearable features are then calculated according to the following definition:

Reference Points on PPG (RP, 1$\sim$10) = {PPG$_{valley}$, sdPPG$_a$, dPPG$_{peak}$, sdPPG$_b$, PPG$_{peak}$, sdPPG$_c$, sdPPG$_d$, dPPG$_{valley}$, sdPPG$_e$, sdPPG$_f$, PPG$_{valley_next}$}

Pulse Transit Time (PTT) = RP$_m$ - R_peak, m = 1$\sim$10

Time Duration (TD) = RRI, RP$_n$ - RP$_m$, $1 \leq m < n \leq 10$

Amplitude alteration (AA) = PPG(RP$_n$) - PPG(RP$_m$), $1 \leq m < n \leq 10$

TABLE I
CATEGORIZATION AND DEFINITION OF WEARABLE FEATURES

Index	Categorization	Definition
1-10	Pulse Transit Time (PTT)	Time difference between R peak in ECG and corresponding reference points in PPG
11-66	Time Duration (TD)	Time duration between two reference points in PPG
67-76	Pulse Width (PW)	Pulse width of PPG, measured at 50%, 60%, 70% amplitude or reference points
77-131	Amplitude Alteration (AA)	Amplitude alteration between 2 reference points in PPG
132-150	Intensity of pulse (AI)	Absolute intensity of PPG, dPPG and sdPPG at reference points
151-204	Area (AR)	Area beneath the curve of PPG signal between 2 reference points
205-222	Relative Index (RI)	Physiological meaningful ratio indices

TABLE II
INDEPENDENCE AND CONDITIONAL INDEPENDENCE RELATIONSHIP OF UNSHIELDED TRIPLE

Hypothesis	chain $X \to Z \to Y$	fork $X \leftarrow Z \to Y$	collider $X \to Z \leftarrow Y$
$X \perp Y$	F	F	T
$X \perp Y \mid Z$	T	T	F

Note: T, F indicates the hypothesis is true or false respectively.

Absolute Intensity of PPG (AI_{PPG}) = PPG(RP_m), m = 1∼10

Absolute Intensity of dPPG (AI_{dPPG}) = dPPG(RP_m), m = 1∼10

Absolute Intensity of sdPPG (AI_{sdPPG}) = sdPPG(RP_m), m = 2, 4, 7∼10

Area under PPG curve (AR) = $\int_{RP_m}^{RP_n}$PPG-AI_{PPG}(PPG_{valley})dt, $1 \le m < n \le 10$

Pulse Width (PW) = t_2 - t_1, $PPG(t_1) = PPG(t_2) = \{AI_{PPG}$, $[AI_{PPG}(RP_5)$-$AI_{PPG}(RP_1)]$*{50%, 60%, 70%}} and $t_1 < t_2$

Physiological Ratio Index (RI): Several physiological meaningful ratio indices [29].

B. Algorithm and Strategy of Causal Inference

1) FCI Algorithm: Assuming the causal Markov and faithfulness, constraint-based algorithms employ the conditional independence tests to infer the causal relationship from observed data [19]. The identification of unshielded triples forms the foundational basis of constraint-based algorithms, which depends on the distinctions of the independence and the conditional independence among them. However, constrain-based methods could not distinguish between chain and fork further, as demonstrated in Table II. That's why the constrain-based methods get a Markov equivalence class, in which the direction of some edges is not oriented.

The identification of unshielded triples could help eliminate the false causality arising from indirect causes and common causes. For instance, the lack of independence between variables *X* and *Y* does not necessarily imply a genuine causal relationship between them. When a variable *Z* exists such that *X* and *Y* are independent given *Z*, it signifies the existence of a chain or fork structure among them.

This study employs the FCI algorithm to infer an initial causal graph, and we describe the step-by-step process of the FCI algorithm as follows:

1) *Initial skeleton identification:* The initial skeleton is identified by iteratively performing a conditional independence test. The edge between variables *X* and *Y* will be deleted if $X \perp Y \mid Z$, where *Z* is the conditional variable set.
2) *Colliders recognition:* If $X \perp Y$ and $X \not\perp Y \mid Z$, it is recognized as a collider within the initial skeleton, represented as $X \longrightarrow Z \longleftarrow Y$.
3) *Possible d separation (PDS) recognition:* Within the graph $\mathcal{G}$, node $X_k \in \text{PDS}(\mathcal{G}, X_i)$, if and only if there exists a path between X_k and X_i where any subpath (X_m, X_l, X_h) is a collider or they form a triangle.
4) *Final skeleton identification:* Delete the edge between *X* and *Y*, if $X \perp Y \mid \text{PDS}(\mathcal{G}, X)$. Then conduct the test for each edge within the initial skeleton to derive the final skeleton.
5) *Orienting:* Orienting the colliders within the final skeleton, and then calibrating the direction through rules [30].

2) CGNN Algorithm: The result inferred by constraint-based algorithms is a Markov equivalence class, in which some edges are not oriented. Inspired by distributional asymmetries of variate [31], the CGNN algorithm leverages generative neural networks to modify and orient the edges of the Markov equivalence class.

With the outstanding representational capability of generative neural networks, the CGNN algorithm could learn the causal relation of FCM with arbitrary accuracy. FCM takes a triplet $C = (\mathcal{G}, f, \varepsilon)$ to describe the causal relation upon a random variable vector $X = (X_1, X_2, \ldots)$, where C represents a set of equations:

$$X_i \leftarrow f_i(X_{Pa(i;\mathcal{G})}, E_i), E_i \sim \varepsilon, i = 1, \ldots, d \tag{1}$$

In formula (1), X_i denotes a node in a causal graph $\mathcal{G}$, f_i describes the causal mechanism between parental nodes $Pa(i;\mathcal{G})$ and X_i, and the noise variables E follow the non-Gaussian distribution and are independent of each other. Given the assumptions of distributional asymmetries in noise variables, conventional FCM-based methods, such as the Linear Non-Gaussian Acyclic Model (LiNGAM), employ ICA to recover the causal relation [21].

CGNN algorithm learns the function f_i on FCM through the generative neural network, and it is trained using backpropagation to minimize the discrepancy between the observational and generated data, measured by the Maximum Mean Discrepancy (MMD) [32]. Further, it identifies the direction of cause and effect by selecting the corresponding 2-variable CGNN with a

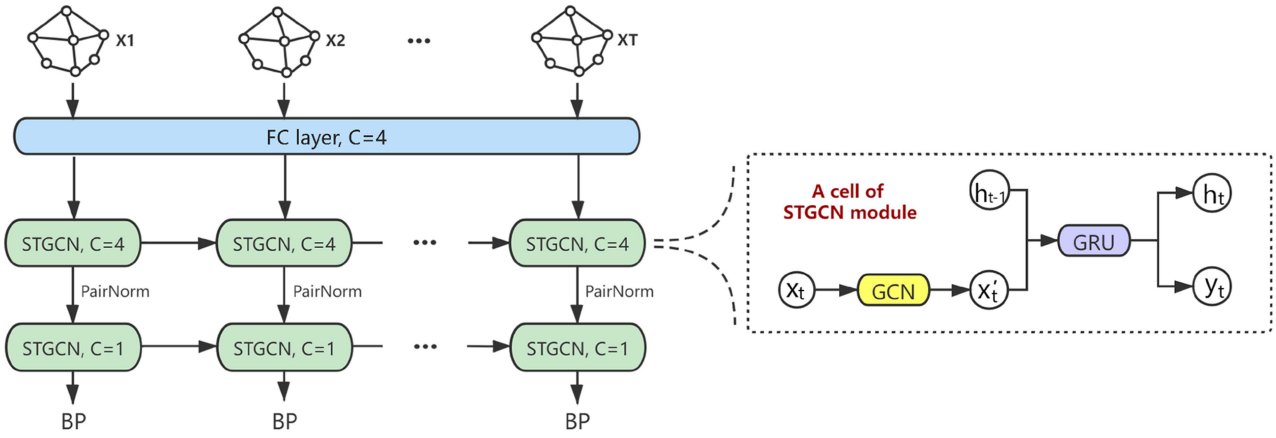

Fig. 3. Structure of the proposed spatiotemporal graph neural network (STGNN) model for causality inspired cuffless continuous BP estimation. The STGNN architecture integrates several key components, including a fully connected (FC) layer for initial feature extraction, a PairNorm layer to address over-smoothing concerns, and two layers of spatiotemporal graph convolutional network (STGCN) modules. These STGCN modules are composed of a graph convolutional network (GCN) for capturing spatial information and a Gated Recurrent Unit (GRU) for capturing temporal information.

smaller MMD, and employs a greedy procedure to orient and modify $\mathcal{G}$:

- Orient each $Xi - Xj$ in $\mathcal{G}$ as $X_i \rightarrow Xj$ or $Xj \leftarrow Xi$ by taking the smaller MMD of the corresponding 2-variable CGNN.
- Traverse paths begin with random nodes until all nodes are visited. Reverse edges directed toward visited nodes once they have revealed cycles.
- Iteratively reversing the edge with a lower MMD, in the meanwhile avoiding cycles.

3) Majority Strategy for Causal Inference: Individual physiological variations could lead to different causal graphs when applying the causal inference algorithm independently for each participant. This study proposes the majority strategy of causal inference for obtaining a universal causal graph applicable to the majority of participants. From the universal causal graph, we wish to draw some general novel insights from the universal causal graph for cuffless continuous BP estimation further.

When employing the FCI algorithm, the majority principle is applied in the context of conducting conditional independence tests. If the test $X \; ? \; Y \mid Z$ needs to be conducted during the iteration of the FCI algorithm, it is performed respectively on each participant in the dataset. Then, by applying the majority strategy, a general conclusion of the test $X \; ? \; Y \mid Z$ is derived based on the agreement of more than half of the participants.

When utilizing the CGNN algorithm, the majority principle is reapplied to the adjacent matrix of the causal graph identified by CGNN. Once obtaining the initial causal graph by FCI algorithm, CGNN algorithm operates individually for each participant, drawing the respective adjacent matrix. Finally, the universal causal graph's adjacency matrix is then derived by applying the majority strategy, where each element in the adjacency matrix of the final causal graph is determined by the majority agreement of the corresponding elements across all the participants' adjacency matrices.

C. Bridging the Gap: Integrating Causal Graph and BP Estimation

1) Spatio-Temporal Graph Neural Network (STGNN): Note that the nodes exhibit complex spatial dependency within the causal graph, while the cardiovascular system demonstrates strong dynamic temporal dependency. On the one hand, the underlying physiological mechanism that governs the causal graph remains elusive, and the spatial dependency between nodes has not yet been distinctly revealed. On the other hand, the BP value in the current cardiac cycle could be influenced by the states of the preceding cardiac cycles. For instance, deep breathing or vigorous exercise could result in improved BP in following cardiac cycles. The pronounced temporal dynamics of cardiovascular system present huge challenges in accurately estimating BP solely based on the information from the current cycle.

Given these challenges, we develop a STGNN model for cuffless continuous BP estimation with the identified causal graph as prior knowledge. As illustrated in Fig. 3, the STGNN model initially employs a shared fully connected (FC) layer for preliminary feature extraction. Further, it incorporates two layers of the spatio-temporal graph convolutional network (STGCN) module to extract complex spatio-temporal features for accurate cuffless continuous BP estimation. The STGCN module can effectively capture the spatial topological properties within the causal graph by utilizing graph convolutional network (GCN), while obtaining the temporal pattern with gated recurrent unit (GRU) [33]. To mitigate the over-smoothing problem, a PairNorm regularization layer [34] is introduced between the STGCN layers.

2) Benchmark Methods: To validate the efficacy of our method, we compare the proposed CiGNN with four state-of-the-art benchmark methods (including knowledge-based, data-driven, and knowledge-data fusion method), as well as three ablation methods. The comparison methods are elaborated as below:

- *Knowledge-based#1:* We compared the CiGNN with two most commonly studied knowledge-based methods. The first knowledge-based method [7] estimates SBP and DBP in terms of relative PTT change by the following equations, where SBP_0, DBP_0 and PTT_0 represents the corresponding initial calibrated value, and γ is a correction factor.

$$SBP = SBP_0 - \frac{2}{\gamma PTT_0}(PTT - PTT_0) \quad (2)$$

$$DBP = DBP_0 - \frac{2}{\gamma PTT_0}(PTT - PTT_0) \quad (3)$$

- *Knowledge-based#2:* The second knowledge-based method [35] estimates SBP and DBP relying on the following equations, where PP_0, MBP_0 and PTT_0 represents the initial calibrated value of pulse pressure (PP), mean blood pressure (MBP) and PTT, and γ is a correction factor.

$$SBP = DBP + PP_0\left(\frac{PTT_0}{PTT}\right)^2 \quad (4)$$

$$DBP = MBP_0 + \frac{2}{\gamma}\ln\frac{PTT_0}{PTT} - \frac{1}{3}PP_0\left(\frac{PTT_0}{PTT}\right)^2 \quad (5)$$

- *Data-driven method:* Tanveer et al. [12] proposed a waveform-based data-driven model for BP estimation. It utilizes a neural network to extract features from ECG and PPG waveforms directly, then taking LSTM layers for SBP and DBP estimation.
- *Fusion-based method:* Hajj et al. [36] proposed a BP estimation method integrating knowledge and data-driven. Initially, they extracted several experiential features from PPG signal, and subsequently constructed a bi-directional neural network for BP estimation.
- *Granger Causality based (GC-based) method:* Drawing inspiration from Granger causality [37], our previous work [14] reported a time-lagged causal links based model for cuffless continuous BP estimation, where the time-lagged causal links were extracted from the causal graph. Since this baseline model only extracts the rough spatio-temporal information, it could be used to validate the efficacy of the proposed CiGNN model.
- *GCN-based method:* To verify CiGNN's efficacy of mining temporal features, this study builds a GCN-based ablation model. According to the idea of control variates, the GCN-based model initially takes a FC layer for preliminary feature extraction. Subsequently, it incorporates two layers of GCN to extract spatial features within the causal graph for cuffless continuous BP estimation, and a PairNorm regularization layer is also introduced between the GCN layers.
- *GRU-based method:* We also construct a GRU-based model for evaluating the ability of mining spatial information of CiGNN. The GRU-based model takes the concatenation of wearable features within the causal graph as its input, as the GRU architecture is unable to process graph-structured data. Likewise, the GRU-based model incorporates a FC layer for initial feature extraction. Furthermore, it integrates two layers of the GRU module to capture temporal features from proceeding continuous cardiac cycles.

3) Model Implementation: We set the sequence length as ten cardiac cycles for STGNN and GRU-based models, and the batch size is configured to 32. Adam optimizer and Cosine Annealing are employed for model training, and the initial learning rate and training epoch are specified as 0.01 and 300. The leave-one-subject-out cross-validation (LOOCV) strategy is employed to evaluate the performance of the proposed methods and baselines, according to the clinical practice.

D. Data Analysis and Model Evaluation

The causal graph is a statistic result derived from statistical tests and scoring rules essentially. In order to verify its accuracy and efficacy, this study employs the analysis of the power spectrum density (PSD) for BP and its causal features, which are the wearable features linking with BP directly within the causal graph. Accounting for the unevenly sampling character of BP and its causal indicators, the Lomb-Scargle algorithm [38] is employed for computing the PSD spanning from 0 to 0.6 Hz.

This study evaluates the proposed cuffless continuous BP estimation model by two international standards, including the Association for the Advancement of Medical Instrumentation (AAMI) [39] and the IEEE Standard for Wearable Cuffless Blood Pressure Measuring Devices (IEEE 1708) [40]. The AAMI and IEEE 1708 standards employ mean error (ME), standard deviation of error (SDE) and mean absolute difference (MAD) to quantitatively assess the model performance. The agreement between the estimated and reference BP values is assessed through the utilization of a Bland-Altman plot, with the agreement limits defined as mean $\pm$ 1.96 $\times$ SD. Furthermore, the statistical significance is evaluated utilizing Student's t-test, employing a significance threshold of $p < 0.05$.

III. Results

A. Causal Graphs

The causal graphs identified with the FCI algorithm and CGNN algorithm are illustrated in Figs. 4 and 5, respectively. For the identified causal graphs, we only present the connected components that contain SBP and DBP. In the causal graph, except for SBP and DBP, each node denotes a specific wearable feature, and the directed arrows between nodes represent the relationship of cause and effect.

The FCI algorithm could not determine the direction of certain edges, so that the circle 'o' are employed to represent the uncertainty in Fig. 4. The circle 'o' signifies that it could be the arrowhead or tail for this edge. The red markers with in Fig. 4 visually highlight the distinction between Figs. 4 and 5. The CGNN algorithm orients all the undirected edges in Fig. 4 and changes the direction of certain edges. Moreover, it eliminates three edges that have been inferred by FCI algorithm.

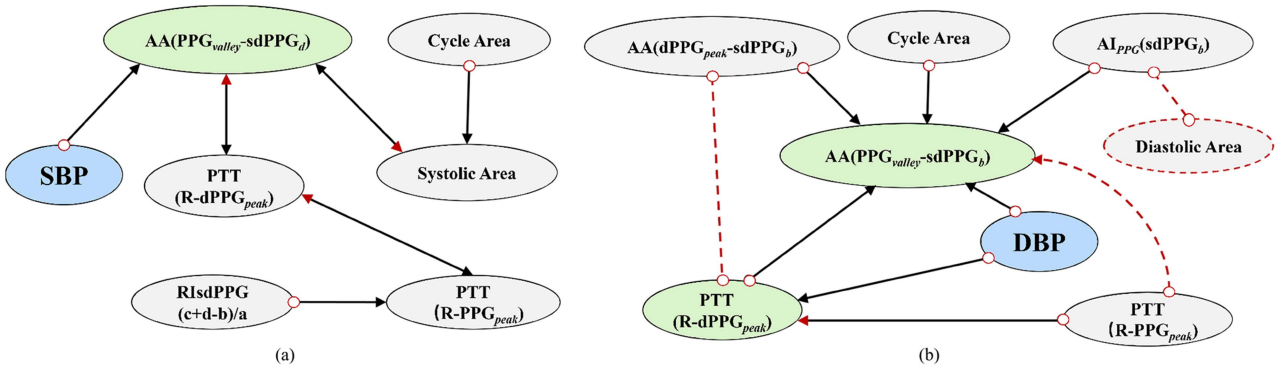

Fig. 4. Connected branches containing (a) SBP and (b) DBP within the initial causal graph obtained by the FCI algorithm, with a distinction between Figs. 4 and 5 visually highlighted by the red markers.

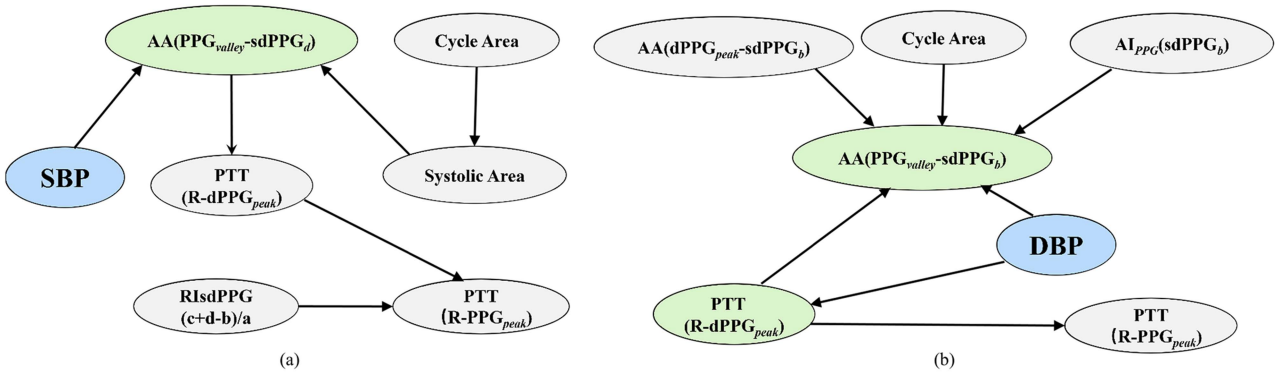

Fig. 5. Connected branches containing (a) SBP and (b) DBP within the causal graph obtained by the CGNN algorithm, with BP depicted in blue and its causal indicators depicted in purple.

The causal graph presents novel indicators that offer valuable insights and inspirations for cuffless continuous BP estimation. Within the causal graph, PTT(R-dPPG$_{peak}$) emerges nearer causal connection with SBP and DBP than PTT(R-PPG$_{peak}$). Furthermore, the causal graph offers an innovative approach concerning the Amplitude Alteration (AA), in which AA refers to the amplitude alteration of PPG signals between two fiducial points, as illustrated in Fig. 2. Within the causal graph, AA(PPG$_{valley}$-sdPPG$_d$) is the effect of SBP, and AA(PPG$_{valley}$-sdPPG$_b$) and PTT(R-dPPG$_{peak}$) are the effects of DBP.

B. Causal Feature Analysis

Within the causal graph, we detected the AA(PPG$_{valley}$-sdPPG$_d$), AA(PPG$_{valley}$-sdPPG$_d$) and PTT(R-dPPG$_{peak}$) that exhibit a direct causal link with BP. As a result, these three wearable features were considered as causal indicators of BP. To demonstrate the capability of these features in tracking BP changes, we conducted power spectrum analysis for these causal features and BP.

Fig. 6 illustrates the temporal variations of SBP, DBP and their corresponding causal indicators. Fig. 7 depicts the paired normalized power spectrum density correspondingly. Evidently, SBP exhibits both slow and fast variations, whereas DBP primarily demonstrates slow variation. SBP demonstrates variability in the low-frequency (LF) domain from 0 to 0.1 Hz, with high-frequency (HF) variation revealed between 0.3 and 0.4 Hz, while DBP predominantly concentrates on LF of 0–0.1 Hz. And this aligns with previous studies on BP variations [8].

The PSD of PTT(R-dPPG$_{peak}$) predominantly concentrates on the HF component, which closely resembles the fast variation pattern observed in SBP, while diverging from the PSD of DBP. However, AA(PPG$_{valley}$-sdPPG$_d$), the causal indicator of SBP, provides a better representation of both the HF and LF components of SBP. Likewise, the PSD of DBP exhibits a significant similarity with its corresponding causal indicator, AA(PPG$_{valley}$-sdPPG$_b$), in LF domain.

The spectral analysis results are in accordance with the causal graph, providing qualitative evidence to support the validity of the identified causal relation. This study further quantitatively analyzes the PSD of SBP, DBP and its corresponding causal indicators. The following three ratios are calculated: the ratio of the area under the power spectrum in the LF band to the area under the power spectrum in the HF band ($\frac{area(LF)}{area(HF)}$), the ratio of the area under the power spectrum in the LF band to the total area under the power spectrum ($\frac{area(LF)}{area(LF+HF)}$), and the ratio of

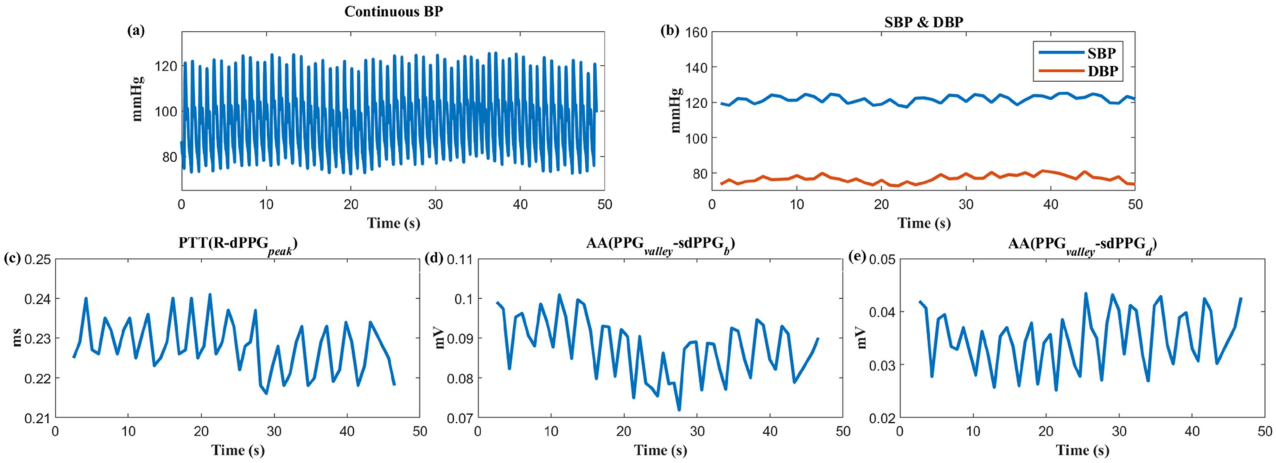

Fig. 6. (a) Continuous BP signal, (b) variations of SBP and DBP, with (c)–(e) variations of three causal indicators of BP.

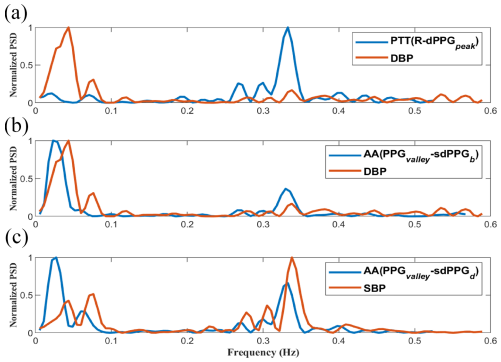

Fig. 7. Paired normalized power spectrum density (PSD) of SBP, DBP and their corresponding causal indicators (a)–(c).

TABLE III
QUANTITATIVE ANALYSIS OF SBP, DBP AND ITS CORRESPONDING CAUSAL INDICATORS' PSD

Index	$\frac{area(LF)}{area(HF)}$	$\frac{area(LF)}{area(LF+HF)}$	$\frac{area(HF)}{area(LF+HF)}$
SBP	0.63	0.39	0.61
DBP	6.32	0.86	0.14
PTT(R-dPPG$_{peak}$)	0.17	0.15	0.85
AA(PPG$_{valley}$-sdPPG$_d$)	0.70	0.41	0.59
AA(PPG$_{valley}$-sdPPG$_d$)	1.82	0.65	0.35

the area under the power spectrum in the HF band to the total area under the power spectrum ($\frac{area(HF)}{area(LF+HF)}$).

The three ratios are computed individually for each participant in the dataset and then averaged, as depicted in Table III. Note that the three ratios of SBP and AA(PPG$_{valley}$-sdPPG$_d$), as well as DBP and AA(PPG$valley$-sdPPG$_b$), exhibit high similarity, which further indicates the validity of the causal graph.

C. Evaluation of BP Estimation Methods

In this subsection, we firstly compare the overall performance between CiGNN and 7 benchmark methods on the internal dataset [26] and the extra VitalDB dataset [27]. Then, on the VitalDB dataset, we assess the performance of these methods for 4 different age groups separately, and comparisons are also analyzed for normotensive and hypertensive subjects, respectively. Finally, we present these methods' capability of tracking BP changes elicited by various maneuvers, i.e., sit (SIT), deep breathing (DB), supine (SUP) and active standing (AS) on the second extra dataset [28].

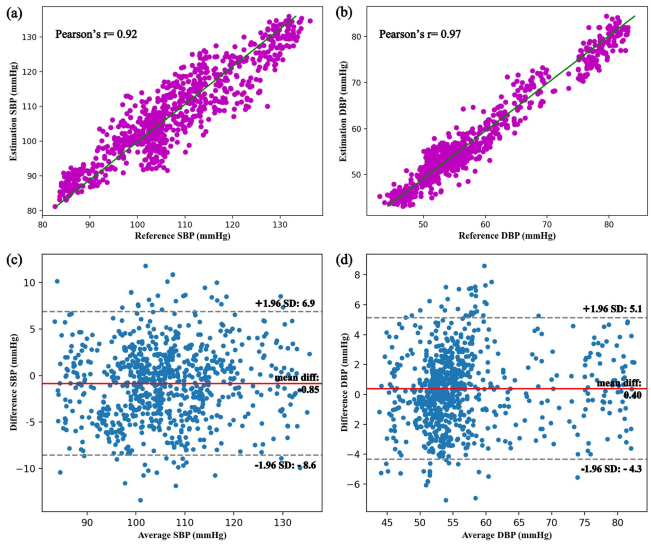

Fig. 8. Correlation, Bland-Altman plots of SBP (a), (c) and DBP (b), (d) of the proposed CiGNN method.

1) Evaluating on the Internal Dataset: On the internal dataset, Fig. 8 depicts the scatter and Bland-Altman plot for SBP and DBP estimation, in which the proposed CiGNN method's estimation results were compared to the reference BP measured by Finapres. The Pearson correlation coefficients between the overall estimated BP values and the reference are 0.92 and 0.97 for SBP and DBP, respectively. In the Bland-Altman plot, the red solid line indicates the bias, while the limits of agreement are

TABLE IV
METHOD PERFORMANCE EVALUATED BY AAMI STANDARD AND IEEE 1708 STANDARD ON THE INTERNAL DATASET

Method	SBP		DBP	
	ME ± SDE (mmHg)	MAD (mmHg)	ME ± SDE (mmHg)	MAD (mmHg)
Knowledge-based#1	-4.89 ± 8.23	12.54	4.15 ± 7.44	7.72
Knowledge-based#2	-4.89 ± 6.01	7.18	3.01 ± 4.86	5.47
Data-driven	-3.30 ± 5.39	5.24	2.56 ± 4.18	4.02
Fusion-based	0.95 ± 4.24	4.62	-0.27 ± 3.54	2.61
GC-based	0.43 ± 6.44	5.10	0.57 ± 3.89	3.05
GCN-based	-2.43 ± 5.46	4.52	**-0.18** ± 2.91	2.26
GRU-based	-2.07 ± 4.38	3.97	0.63 ± 2.75	2.04
The proposed CiGNN	**-0.85** ± **3.94***	**3.20***	0.40 ± **2.41***	**1.85***

Note: AAMI standard requires mean error (ME) <5 mmHg and standard deviation of error (SDE) <8 mmHg.
IEEE 1708 standard requires mean absolute difference (MAD) <6 mmHg.
* indicates significant difference compared with other methods.
Bold values is the minimum value in each column.

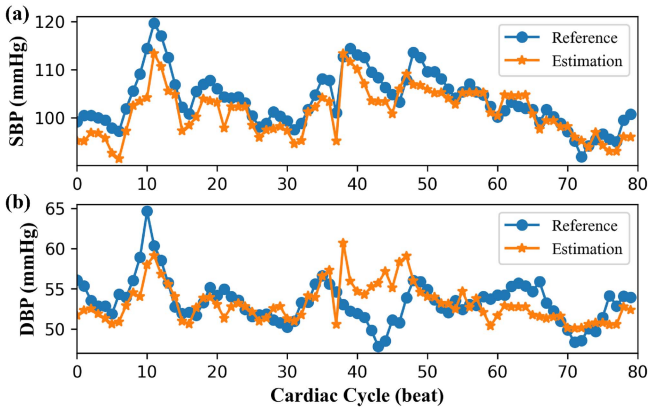

Fig. 9. Estimated beat-to-beat SBP (a) and DBP (b) of the proposed CiGNN method with corresponding reference Finapres BP.

depicted by the black dash-dot lines (bias ±1.96× SD). We can observe that the majority of data points fall within the limits of agreement, demonstrating a close consistency between the BP estimated by the proposed CiGNN method and the Finapres' measurements. The bias values for SBP and DBP estimation are −0.85 mmHg and 0.40 mmHg, respectively.

Furthermore, Fig. 9 depicts a representative example of the beat-to-beat comparison between the reference BP of Finapres and the estimation BP by the proposed CiGNN method. The average values of SBP and DBP measured by the Finapres are 103.51±7.04 mmHg and 54.03±6.60 mmHg, respectively. And the proposed CiGNN model estimated the average values of SBP and DBP are 103.16±7.06 mmHg and 53.61±6.52 mmHg, respectively. It is evident that the estimation demonstrates a remarkable ability to accurately track the intensely oscillating reference BP.

The evaluation results of AAMI and IEEE 1708 standards for the proposed method and baselines are shown in Table IV. Note that the CiGNN method demonstrates commendable performance across multiple evaluation indicators, with ME ± SDE values being −0.85 ± 3.94 mmHg and 0.40 ± 2.41 mmHg, as well as MAD values being 3.20 mmHg and 1.85 mmHg for SBP and DBP, respectively. The performance of the CiGNN model surpasses that of benchmark methods with statistical significance ($p < 0.05$), providing strong evidence for its efficacy in capturing spatio-temporal information for cuffless continuous BP estimation.

2) Evaluation on the Extra VitaDB Dataset: On the VitalDB, the overall performance of CiGNN as well as comparison methods are evaluated on 205 subjects (103 normotensive and 102 hypertensive) with age ranging from 20 to 90. Table V presents the evaluation results of AAMI and IEEE 1708 standards for CiGNN and comparison methods. The CiGNN model demonstrates commendable performance across multiple evaluation metrics, with ME ± SDE values being −0.37 ± 4.30 mmHg and −0.84 ± 3.15 mmHg, as well as MAD values being 4.15 mmHg and 2.79 mmHg for SBP and DBP, respectively. Note that the proposed CiGNN achieves smaller ME, SDE, as well as MAD for BP estimation, and the difference is significant.

To validata the robustness of the proposed method, we analyze its performance from the perspectives of patient age and whether they have hypertension. And the brief statistic information is illustrated in Tables VI and VII. The VitalDB dataset was divided into four age groups. As shown in Fig. 10, the performance of these methods with subjects at different age groups are analyzed. We evaluate those methods' performance through MAD of the estimated BP. In general, BP of the patients aged 60–80 is the most difficult to estimation, as the MAD of each method is high at this age stage. And for patients aged from 20 to 40, the estimation of BP is relatively easy. Note that the performance of those methods varied at different age groups. It is noteworthy that the CiGNN method performs stably and excellently across different age stages, surpassing other comparison methods.

As presented in Fig. 11, these methods' performance are evaluated for the normotensive group and the hypertensive group, respectively. Due to the complexity of BP changes in people with hypertension, it is difficult to track and estimate their blood pressure compared with normotensive group. The mean SBP and DBP of 103 nomotensive subjects are 112.81 ± 15.65 and 56.99 ± 7.96, while the mean SBP and DBP for 102 hypertensive subjects are 139.30 ± 19.67 and 74.00 ± 8.71, respectively.

Fig. 11 depicts the performance of CiGNN and comparison methods by ME ± SDE. We could see that the SDE of hypertensive group are higher than that of normotensive group for all the methods, indicating that the BP estimation for hypertensive subjects might be more challenging. The discrepancies are especially obvious in SBP estimation. The proposed CiGNN performs better than other methods not only for the normotensive

TABLE V
METHOD PERFORMANCE EVALUATED BY AAMI STANDARD AND IEEE 1708 STANDARD ON THE VITALDB DATASET

Method	SBP		DBP	
	ME ± SDE (mmHg)	MAD (mmHg)	ME ± SDE (mmHg)	MAD (mmHg)
Knowledge-based#1	-4.59 ± 12.19	14.73	-4.26 ± 5.10	4.53
Knowledge-based#2	**0.13** ± 7.24	8.68	-1.34 ± 5.36	6.95
Data-driven	0.72 ± 8.18	7.77	-2.91 ± 5.59	6.14
Fusion-based	-1.96 ± 5.29	5.32	-1.61 ± 3.89	3.76
GC-based	-0.25 ± 5.76	5.43	**-0.02** ± 4.40	4.63
GCN-based	-3.46 ± 6.06	4.92	-0.04 ± 4.10	5.36
GRU-based	1.22 ± 4.81	5.08	-0.34 ± 3.63	3.29
The proposed CiGNN	-0.37 ± **4.30***	**4.15***	-0.84 ± **3.15***	**2.79***

Note: AAMI standard requires mean error (ME) <5 mmHg and standard deviation of error (SDE) <8 mmHg.
IEEE 1708 standard requires mean absolute difference (MAD) <6 mmHg.
* indicates significant difference compared with other methods.
Bold values is the minimum value in each column.

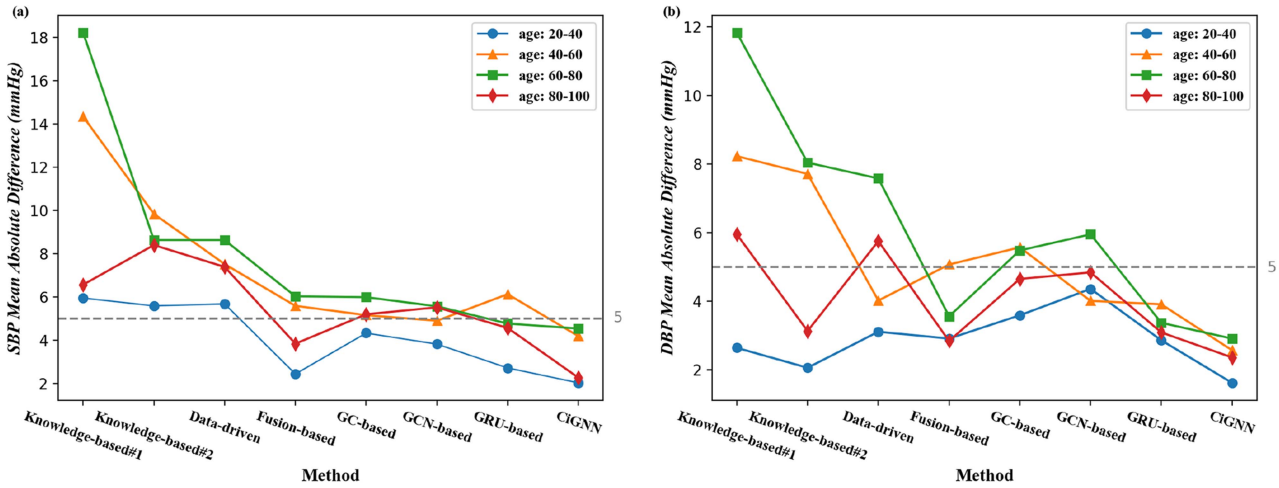

Fig. 10. Performance of BP estimation with the proposed and comparison methods under four different age groups for (a) SBP and (b) DBP.

TABLE VI
SUBJECTS' CHARACTERISTICS OF THE VITALDB DATASET

Age groups	20-40(n=28)	40-60(n=79)	60-80(n=92)	80-100(n=6)
Gender (M/F)	17/11	46/33	68/24	2/4
BMI (Kg/m^2)	19.9 ± 3.5	22.9 ± 3.8	23.2 ± 3.2	21.1 ± 3.6
SBP (mmHg)	117.91 ± 13.25	136.96 ± 18.52	120.11 ± 20.84	109.29 ± 16.56
DBP (mmHg)	77.80 ± 6.83	65.85 ± 8.36	59.76 ± 9.14	57.54 ± 8.16

TABLE VII
NORMOTENSIVE VS. HYPERTENSIVE GROUP INFORMATION OF THE VITALDB DATASET

	All Subjects (n=205)	Normotensive Group (n=103)	Hypertensive Group (n=102)
Gender (M/F)	133 / 72	65 / 38	68/34
Mean Age (range)	57 (20-90)	54 (20-90)	61 (22-86)
BMI (Kg/m^2)	22.6 ± 3.7	22.1 ± 3.9	23.0 ± 3.5
SBP (mmHg)	125.99 ± 4.36	112.81 ± 15.65	139.30 ± 19.67
DBP (mmHg)	64.51 ± 9.73	56.99 ± 7.96	74.00 ± 8.71

group but also for the hypertensive group, and the difference is significant. For normotensive group, the ME ± SDE of estimated SBP and DBP with the CiGNN method are -0.59 ± 3.35 mmHg and 0.69 ± 2.45 mmHg, respectively. And for hypertensive group, the corresponding ME ± SDE of estimated SBP and DBP are 1.66 ± 4.61 mmHg and 0.91 ± 3.32 mmHg, respectively.

TABLE VIII
COEFFICIENT OF VARIATION (CV) OF FOUR MANEUVERS FOR SBP AND DBP ON THE EXTRA DATASET [28]

Maneuvers	SBP		DBP	
	Mean ± SD	CV	Mean ± SD	CV
Sit, SIT	127 ± 8.3	0.0654	77 ± 5.3	0.0688
Deep breathing, DB	132 ± 11.5	0.0871	80 ± 8.2	0.1025
Supine, SUP	129 ± 14.6	0.1132	74 ± 9.4	0.1270
Active standing, AS	140 ± 19.1	0.1364	85 ± 12.6	0.1482

3) Comparison of Different Maneuvers: It is crucial for cuffless continuous BP estimation algorithm to accurately track the BP changes due to external interventions. So we employ the second extra dataset [28] with BP changes induced by different maneuvers to validate CiGNN's ability of tracking BP changes.

This work utilizes coefficient of variation (CV) to assess the magnitude of BP changes under different maneuvers. The definition of CV is depicted in following formula (6), where μ is the mean value of BP and δ is the standard deviation of BP.

$$CV = \frac{\delta}{\mu} \tag{6}$$

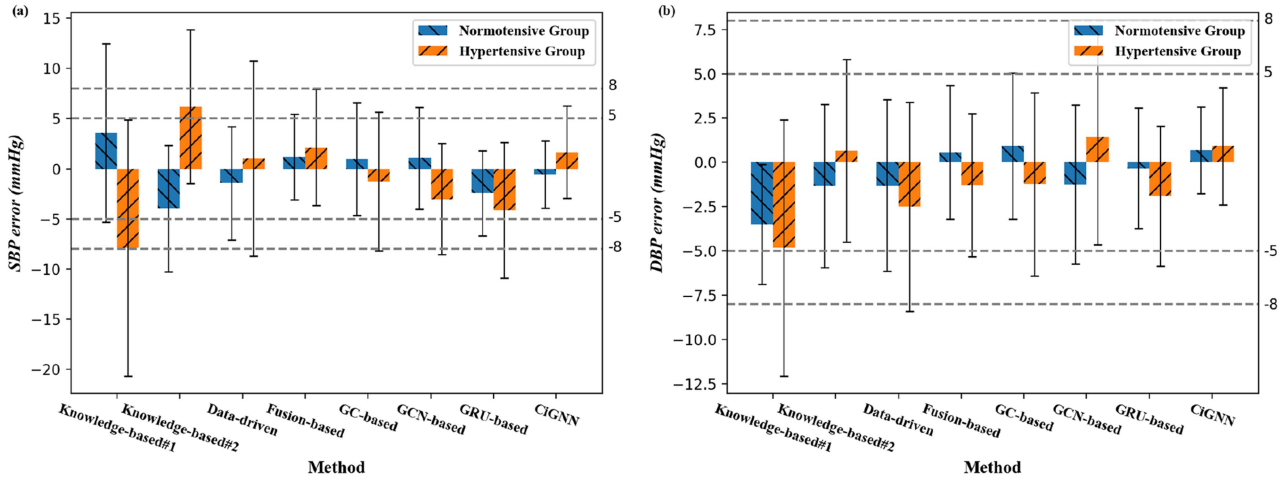

Fig. 11. Performance evaluation of BP estimation with the proposed and comparison methods in normotensive group and hypertensive group for (a) SBP and (b) DBP.

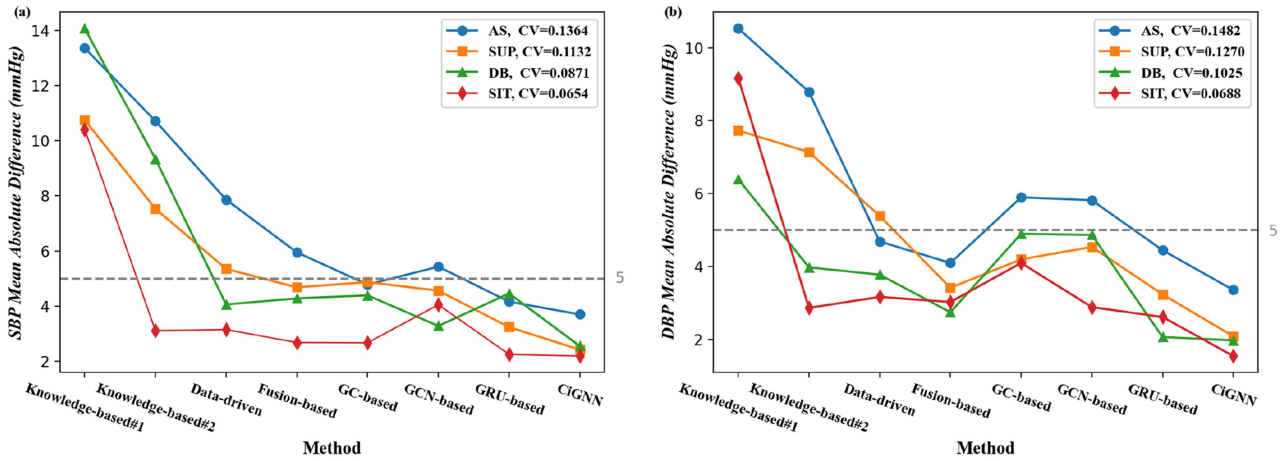

Fig. 12. Performance of BP estimation with the proposed and comparison methods under four various maneuvers with coefficient of variation (CV) of the BP indicated for each maneuver. (a) SBP and (b) DBP.

Table VIII presents the CV of four maneuvers for SBP and DBP, where the ranking of the magnitude of BP changes is: SIT <DB <SUP <AS.

Fig. 12 evaluates the performance of proposed CiGNN and other comparison methods under four various maneuvers by means of the estimated BP's MAD. Note that the higher CV, the more difficult it is to estimate the BP, and the performance of thoes methods differed across various maneuvers. The proposed CiGNN method achieves the best performance under four maneuvers compared with other methods, and the difference is significant.

IV. Discussion

This study investigated the feasibility of integrating the causal knowledge with GNN for cuffless continuous BP estimation. We developed a two-stage causality inspired and GNN based framework that can extract causal features and learn both spatial and temporal patterns from the causal graph sequence for better cuffless continuous BP estimation. By employing FCI and CGNN algorithms, the causal relationship between wearable features and BP was depicted via a causal graph. Remarkably, the causal features linked with BP within the causal graph demonstrated excellent capability of tracking BP changes. The introduced STGNN model, with the causal graph sequence as its input, exhibited commendable performance for cuffless continuous BP estimation.

A. Causal Inference

Inferring causal relationships from observed data has drawn substantial attention, predominantly encompassing three method types: constraint-based algorithm, score-based algorithm, and FCM-based algorithm. The score-based algorithm is among the most promising methods. It relies on the assumption

that there is external score-functions capable of detecting various causal relations. Nevertheless, searching for the optimal scoring causal graph across the entire graph space could be computationally expensive, particularly when dealing with a large number of extracted wearable features in this study. Therefore, this study employs the FCI algorithm that is computationally more effective (than the score-based algorithm) to obtain an initial causal graph, i.e., a Markov equivalence class. Then, the CGNN algorithm is utilized to modify and orient the edges of the initial causal graph. In summary, this study balances computational cost and causal inference accuracy by applying two types of causal inference algorithms.

As shown in Fig. 5, this study infers separate causal graphs between SBP, DBP and wearable features, respectively, so that there is no causal graph incorporating both SBP and DBP simultaneously. The notably high interdependence between SBP and DBP limits the inclusion of any other wearable features in their connected branch of the causal graph, if SBP and DBP are not individually taken into account for causal inference. Given the conditional independence relationships: $SBP \perp wearable feature \mid DBP$ and $DBP \perp wearable feature \mid SBP$, the edges connecting SBP or DBP with any wearable features will be removed, as the FCI algorithm iterates.

For two definitions of PTT [41], BP has a closer causal relation with PTT(R-dPPG$_{peak}$) in the causal graph, rather than PTT(R-PPG$_{peak}$). This aligns with the prior studies that PTT(R-dPPG$_{peak}$) are favored over PTT(R-PPG$_{peak}$) for the cuffless continuous BP estimation [42]. In addition, the causal graph suggests new causal indicators, the AA(PPG$_{valley}$-sdPPG$_d$) and AA(PPG$_{valley}$-sdPPG$_b$), for cuffless continuous BP estimation. The power spectrum analysis demonstrates the robust tracking capability of AA(PPG$_{valley}$-sdPPGd) and AA(PPG$valley$-sdPPG$_b$) in capturing BP variations across both LF and HF ranges. In psychology, the LF variation of BP are attributed to respiratory sinus arrhythmia (RSA) [43], indicating respiratory activity [44], while the HF variation are linked to vasomotion waves resulting from oscillations in sympathetic vasomotor tone [45]. Hence, the newly identified causal indicators effectively reveal the psychological modulation of respiration and sympathetic tone on BP.

B. Cuffless Continuous BP Estimation

This study explores the role of utilizing causality for cuffless continuous BP estimation. We creatively propose the STGNN model for bridging the gap between causal graph, representing the causal relation of wearable features and BP, and cuffless continuous BP estimation. This study is a pioneering attempt to incorporate GNN to capture the intricate causal dependent relationship between wearable features and BP within the cardiovascular system, specifically in the context of cuffless continuous BP estimation. Instead, modules like GRU and LSTM have been extensively employed for several years to capture temporal features from continuous cardiac beats [12], [36].

The STGNN model effectively leverages the causal prior knowledge embedded in the causal graph, and results in excellent performance across multiple evaluation metrics. As described in Section III-C, the performance of the STGNN model exhibits statistically significant superiority ($p < 0.05$) over the GRU-based model, which demonstrates the superior ability of STGNN model for mining spatial information embedded within the causal graph. Similarly, compared with the GCN-based model, STGNN also demonstrates a better ability ($p < 0.05$) in extracting temporal information from continuous cardiac beats. And the proposed STGNN model also presents a greater capacity ($p < 0.05$) for mining spatio-temporal information compared to the time-lagged causal links based model.

Moreover, the evaluation results highlight the superiority of temporal information over spatial information for BP estimation, as evidenced by the better performance of the GRU-based model compared to the GCN-based model. This finding is consistent with prior studies that the cardiovascular system exhibits high auto-correlation, whereby the BP value in the current cardiac beat is easily influenced by the states of preceding cardiac beats.

When compared to knowledge-based methods, data-driven method as well as the fusion of knowledge and data-driven method, the proposed CiGNN method demonstrates the best performance on both internal and extra dataset, due to its integration of causal information and superior structural design. For different age groups, various maneuvers and hypertensive group, our CiGNN could achieve excellent estimation of cuffless continuous BP. This proves that the CiGNN method is robust for different condition of BP changes.

C. Limitation

There are several limitations of this study. First, this study only presented the excellent tracking capability of the detected causal indicators for BP variations within the frequency domain. The underlying physiological mechanism between identified causal indicators and BP has not been investigated yet. The other limitation is that the proposed framework consists of two stages, which have not been developed into an end-to-end model. Last, multiple factors, such as age, maneuvers and whether the patient has hypertension, will affect the accuracy of BP estimation. The proposed method has not considered the causal relationship between those factors and BP, and have not utilized it to improve the accuracy of BP estimation.

V. Conclusion & Future Work

In this study, we proposed a two-stage CiGNN framework that integrates causal inference with GNN for cuffless continuous BP estimation. Initially, with two types of causal inference algorithms alongside the majority strategy, we inferred a causal graph depicting the causal relationship between BP and wearable features. The causal graph identified new causal indicators other than PTT that were able to track BP changes effectively. Further, we proposed a STGNN model that bridges the gap between causal graph and BP estimation creatively. With the learned spatio-temporal information by STGNN, we achieved substantial improvement for cuffless continuous BP estimation.

Future study should integrate physiological knowledge to uncover the underlying relationship between causal indicators and

BP, to establish an end-to-end causal-based cuffless continuous BP estimation model, as well as to conduct causal inference analysis on hypertensive subjects. There is also scope for work to better understand how this can be best applied to support the prevention and treatment of hypertension for people, patients and clinicians.

REFERENCES

[1] World Health Organization, *World Health Statistics 2018*. Geneva, Switzerland: WHO, 2018.

[2] P. A. James et al., "2014 evidence-based guideline for the management of high blood pressure in adults: Report from the panel members appointed to the Eighth Joint National Committee (JNC 8)," *J. Cardiopulmonary Rehabil. Prevention*, vol. 311, pp. 507–520, 2014.

[3] Y. Chen et al., "Impact of hypertension prevalence trend on mortality and burdens of dementia and disability in England and wales to 2060: A simulation modelling study," *Lancet Healthy Longevity*, vol. 4, pp. e470–e477, 2023.

[4] W. B. White, T. Giles, G. L. Bakris, J. M. Neutel, G. Davidai, and M. A. Weber, "Measuring the efficacy of antihypertensive therapy by ambulatory blood pressure monitoring in the primary care setting," *Amer. Heart J.*, vol. 151, no. 1, pp. 176–184, 2006.

[5] T. G. Pickering, D. Shimbo, D. Haas, and A. B. P. M. W. Group, "Ambulatory blood-pressure monitoring," *New England J. Med.*, vol. 353, no. 8, pp. 850–851, 2006.

[6] X.-R. Ding et al., "Continuous blood pressure measurement from invasive to unobtrusive: Celebration of 200th birth anniversary of Carl Ludwig," *IEEE J. Biomed. Health Inform.*, vol. 20, no. 6, pp. 1455–1465, Nov. 2016.

[7] W. Chen, T. Kobayashi, S. Ichikawa, Y. Takeuchi, and T. Togawa, "Continuous estimation of systolic blood pressure using the pulse arrival time and intermittent calibration," *Med. Biol. Eng. Comput.*, vol. 38, pp. 569–574, 2000.

[8] X.-R. Ding, Y.-T. Zhang, J. Liu, W.-X. Dai, and H. K. Tsang, "Continuous cuffless blood pressure estimation using pulse transit time and photoplethysmogram intensity ratio," *IEEE Trans. Biomed. Eng.*, vol. 63, no. 5, pp. 964–972, May 2016.

[9] N. Canac, K. Jalaleddini, S. G. Thorpe, C. M. Thibeault, and R. B. Hamilton, "Pathophysiology of intracranial hypertension and noninvasive intracranial pressure monitoring," *Fluids Barriers CNS*, vol. 17, pp. 1–21, 2020.

[10] C. El-Hajj and P. A. Kyriacou, "A review of machine learning techniques in photoplethysmography for the non-invasive cuff-less measurement of blood pressure," *Biomed. Signal Process. Control*, vol. 58, 2020, Art. no. 101870.

[11] F. Miao et al., "Continuous blood pressure measurement from one-channel electrocardiogram signal using deep-learning techniques," *Artif. Intell. Med.*, vol. 108, 2020, Art. no. 101919.

[12] M. S. Tanveer and M. K. Hasan, "Cuffless blood pressure estimation from electrocardiogram and photoplethysmogram using waveform based ANN-LSTM network," *Biomed. Signal Process. Control*, vol. 51, pp. 382–392, 2019.

[13] Y. H. Li, L. N. Harfiya, K. Purwandari, and Y. D. Lin, "Real-time cuffless continuous blood pressure estimation using deep learning model," *Sensors*, vol. 20, 2020, Art. no. 5606.

[14] L. Liu, Y.-T. Zhang, W. Wang, Y. Chen, and X. Ding, "Causal inference based cuffless blood pressure estimation: A pilot study," *Comput. Biol. Med.*, vol. 159, 2023, Art. no. 106900.

[15] J. Pearl and D. Mackenzie, *The Book of Why: The New Science of Cause and Effect*. New York, NY, USA: Basic Books, 2018.

[16] J. Pearl, *Causality: Models, Reasoning and Inference*, vol. 19. Cambridge, U.K.: Cambridge Univ. Press, 2000.

[17] K. Kuang et al., "Causal inference," *Engineering*, vol. 6, no. 3, pp. 253–263, 2020.

[18] R. Guo, L. Cheng, J. Li, P. R. Hahn, and H. Liu, "A survey of learning causality with data: Problems and methods," *ACM Comput. Surv.*, vol. 53, no. 4, pp. 1–37, 2020.

[19] C. Glymour, K. Zhang, and P. Spirtes, "Review of causal discovery methods based on graphical models," *Front. Genet.*, vol. 10, 2019, Art. no. 524.

[20] R. Moraffah et al., "Causal inference for time series analysis: Problems, methods and evaluation," *Knowl. Inf. Syst.*, vol. 63, pp. 3041–3085, 2021.

[21] S. Shimizu, P. O. Hoyer, A. Hyvärinen, A. Kerminen, and M. Jordan, "A linear non-Gaussian acyclic model for causal discovery," *J. Mach. Learn. Res.*, vol. 7, no. 10, pp. 2003–2030, 2006.

[22] J. Runge, P. Nowack, M. Kretschmer, S. Flaxman, and D. Sejdinovic, "Detecting and quantifying causal associations in large nonlinear time series datasets," *Sci. Adv.*, vol. 5, no. 11, 2019, Art. no. eaau4996.

[23] B. Sanchez-Lengeling, E. Reif, A. Pearce, and A. B. Wiltschko, "A gentle introduction to graph neural networks," *Distill*, vol. 6, no. 9, 2021, Art. no. e33.

[24] S. Peter and G. Clark, "An algorithm for fast recovery of sparse causal graphs," *Social Sci. Comput. Rev.*, vol. 9, no. 1, pp. 62–72, 2016.

[25] O. Goudet, D. Kalainathan, P. Caillou, I. Guyon, D. Lopez-Paz, and M. Sebag, "Causal generative neural networks," 2017, *arXiv:1711.08936*.

[26] F. Miao et al., "A novel continuous blood pressure estimation approach based on data mining techniques," *IEEE J. Biomed. Health Inform.*, vol. 21, no. 6, pp. 1730–1740, Nov. 2017.

[27] H.-C. Lee, Y. Park, S. B. Yoon, S. M. Yang, D. Park, and C.-W. Jung, "VitalDB, A high-fidelity multi-parameter vital signs database in surgical patients," *Sci. Data*, vol. 9, no. 1, 2022, Art. no. 279.

[28] X. Ding, B. P. Yan, Y.-T. Zhang, J. Liu, N. Zhao, and H. K. Tsang, "Pulse transit time based continuous cuffless blood pressure estimation: A new extension and a comprehensive evaluation," *Sci. Rep.*, vol. 7, no. 1, 2017, Art. no. 11554.

[29] X. Ding, B. P. Yan, Y.-T. Zhang, J. Liu, P. Su, and N. Zhao, "Feature exploration for knowledge-guided and data-driven approach based cuffless blood pressure measurement," 2019, *arXiv:1908.10245*.

[30] J. Zhang, "On the completeness of orientation rules for causal discovery in the presence of latent confounders and selection bias," *Artif. Intell.*, vol. 172, no. 16/17, pp. 1873–1896, 2008.

[31] C. Heinze-Deml, M. H. Maathuis, and N. Meinshausen, "Causal structure learning," *Annu. Rev. Statist. Appl.*, vol. 5, pp. 371–391, 2018.

[32] A. Gretton, K. Borgwardt, M. J. Rasch, B. Scholkopf, and A. J. Smola, "A kernel method for the two-sample problem," in *Proc. 19th Int. Conf. Neural Inf. Process. Syst.*, 2008, pp. 513–520.

[33] J. Chung, C. Gulcehre, K. Cho, and Y. Bengio, "Empirical evaluation of gated recurrent neural networks on sequence modeling," 2014, *arXiv:1412.3555*.

[34] L. Zhao and L. Akoglu, "PairNorm: Tackling oversmoothing in GNNs," 2019, *arXiv:1909.12223*.

[35] C. Poon and Y. Zhang, "Cuff-less and noninvasive measurements of arterial blood pressure by pulse transit time," in *Proc. 27th Annu. Conf. IEEE Eng. Med. Biol.*, 2006, pp. 5877–5880.

[36] C. El-Hajj and P. A. Kyriacou, "Deep learning models for cuffless blood pressure monitoring from PPG signals using attention mechanism," *Biomed. Signal Process. Control*, vol. 65, 2021, Art. no. 102301.

[37] C. W. Granger, "Investigating causal relations by econometric models and cross-spectral methods," *Econometrica: J. Econometric Soc.*, vol. 37, pp. 424–438, 1969.

[38] T. Ruf, "The Lomb-Scargle periodogram in biological rhythm research: Analysis of incomplete and unequally spaced time-series," *Biol. Rhythm Res.*, vol. 30, no. 2, pp. 178–201, 1999.

[39] M. Prsan, "American national standard for nonautomated sphygmomanometer," *Amer. J. Hypertension*, vol. 8, pp. 210–213, 1995.

[40] *IEEE Standard for Wearable Cuffless Blood Pressure Measuring Devices*, IEEE Standard 1708–2014, 2014.

[41] X.-R. Ding, J. Liu, W.-X. Dai, P. Carvalho, R. Magjarević, and Y.-T. Zhang, "An attempt to define the pulse transit time," in *Proc. Int. Conf. Biomed. Health Inform.*, 2015, pp. 219–221.

[42] X. Ding and Y. Zhang, "Pulse transit time technique for cuffless unobtrusive blood pressure measurement: From theory to algorithm," *Biomed. Eng. Lett.*, vol. 9, pp. 37–52, 2019.

[43] A. Dornhorst, P. Howard, and G. Leathart, "Respiratory variations in blood pressure," *Circulation*, vol. 6, no. 4, pp. 553–558, 1952.

[44] J. A. Taylor and D. L. Eckberg, "Fundamental relations between short-term RR interval and arterial pressure oscillations in humans," *Circulation*, vol. 93, no. 8, pp. 1527–1532, 1996.

[45] A. Malliani, M. Pagani, F. Lombardi, and S. Cerutti, "Cardiovascular neural regulation explored in the frequency domain," *Circulation*, vol. 84, no. 2, pp. 482–492, 1991.